THE JOURNAL OF PHYSICAL CHEMISTRY C
A JOURNAL OF THE AMERICAN CHEMICAL SOCIETY

pubs.acs.org/JPCC

Article

Toward Vibrational Tomography of Citrate on Dynamically Changing Individual Silver Nanoparticles

Tripti Ahuja,[†] Kamalesh Chaudhari,[†] Ganesan Paramasivam, Gopi Ragupathy, Jyoti Sarita Mohanty, and Thalappil Pradeep*

Cite This: *J. Phys. Chem. C* 2021, 125, 3553−3566

Read Online

ACCESS | Metrics & More | Article Recommendations | Supporting Information

ABSTRACT: This study explored changes in binding modes of the most common ligand, citrate on silver nanoparticles (AgNPs) using single-particle surface-enhanced Raman scattering (SP-SERS). Single AgNPs of 50 ± 10 nm diameter anchored on clean glass slides were monitored using time-dependent SP-SERS with 632.8 nm excitation at 1.3 μW incident (0.5 μW absorbed) power per nanoparticle. We observed several distinct spectra of citrate during time-dependent SP-SERS. Analysis of 1400 spectra showed the existence of two major groups termed as favorable (F) and probable (P) spectra based on their likelihood of appearance and intensities. These distinct spectra corresponded to a multitude of binding modes, structures, and variants of photocatalyzed products of citrate on the surface of dynamically changing AgNPs. Density functional theory (DFT) simulations were performed to model the structures and binding modes of citrate on an Ag(111) surface, and corresponding Raman spectra were computed and compared with distinct spectral types. Experiments performed with deuterated (2,2,4,4-d_4) citrate-capped AgNPs provided additional evidence to understand the shifts in vibrational features obtained in SP-SERS of citrate-capped AgNPs. These systematic analyses of time-dependent SP-SERS spectra may be used for the reconstruction and vibrational tomography (VT) of ligands at the single-particle level. The proposed VT approach is similar to sectioning an object through a multitude of orientations and reconstructing its three-dimensional structure, although the structures reconstructed here are molecular orientations.

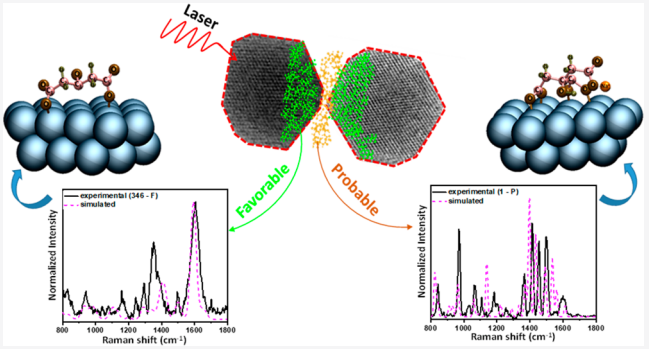

INTRODUCTION

Trisodium citrate (TSC) has been used in the synthesis of colloidal nanoparticles (NPs) and has probably become the most common reducing and stabilizing agent in the history of noble metal nanomaterials.[1−7] This ligand is shown to be important in particle aggregation,[8] ligand exchange reactions,[9] particle growth mechanism,[10] enzyme catalysis reactions,[11] and others. Due to its large implications, it is indeed necessary to explore its structure on the surface of NPs meticulously. TSC, a complex molecule with three carboxylate (COO^-) groups and one α-hydroxyl (α-OH) group, can adopt a variety of structures with different binding modes.[12] Enormous efforts have been made by the scientific community to understand its molecular structure on the surface of NP using various methods.[7,12−19] Munro et al.have performed in-depth studies to understand the formation of TSC-reduced colloids and their surface properties by UV−vis absorption spectroscopy, nuclear magnetic resonance (NMR), and surface-enhanced Raman scattering (SERS).[17] Among all the techniques, SERS serves as a powerful analytical tool for sensitive, qualitative, and semiquantitative analyses. Authors proposed that COO^- of adsorbed citrate (termed as citrate in the discussion below) bind nonequivalently on the Ag surface, where one of the terminal and the central COO^- groups bind to the Ag surface, and the other terminal COO^- remains unbound.[17] Other recent studies[7,12,14,17,19] have also proposed various binding modes of citrate. X-ray photoelectron spectroscopy (XPS) has been used to determine the surface composition and suggested that citrate anions are adsorbed on the surface of AuNPs through the central COO^- group.[16,19] Attenuated total reflectance infrared (ATR-IR) spectroscopy was used to study intermolecular interactions between the adsorbed and dangling citrate anions. Further, dimer and trimer structures of citrate on the AuNPs surface were proposed.[19] Such studies helped to understand the stabilizing nature of ligands used in the preparation of NPs. Other techniques, like atomic force microscopy (AFM),[20] scanning tunneling microscopy (STM),[21] Fourier transform infrared

Received: November 5, 2020
Revised: January 20, 2021
Published: February 4, 2021

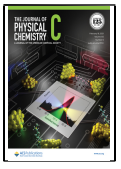

https://dx.doi.org/10.1021/acs.jpcc.0c09981
J. Phys. Chem. C 2021, 125, 3553−3566

spectroscopy (FTIR),[19,22] and solid-state nuclear magnetic resonance (SS-NMR),[15] have also been used to explore the stabilizing nature of citrate. Density functional theory (DFT) and molecular dynamics have been applied to understand the surface coordination of the COO^- of citrate with the NP surface.[12,15] Such studies imparted valuable information on the hydrogen bonding networks between citrate ions,[19] their binding schemes,[13,17] and the effect of aging.[7,16]

In the past decade, single-particle and single-molecule SERS gained large interest in various fields of applications such as catalysis, sensing, live cell imaging, and so on. A study at the single-particle level provides newer and deeper insights about the system under study.[23−27] Despite the large number of investigations[12,15,17,18,21,28] on understanding the nature of citrate on the NP surface, structural details of the species at the surface are still unknown, as such studies are challenging. All the studies mentioned above have been performed on an ensemble of NPs. Although citrate-capped Au and Ag NPs have been used extensively in single-particle and single-molecule SERS studies,[29−31] understanding the binding modes and existence of photocatalyzed products of citrate at a single-particle level are still elusive.

Herein we introduce a technique that couples confocal Raman microspectroscopy (CRM) with dark field microscopy (DFM) to visualize dynamically changing AgNPs under laser irradiation and perform temporal SERS at the single-particle level. Time-dependent single-particle SERS (SP-SERS) measurements were performed on specific AgNPs (showing surface plasmon resonance (SPR), between 640−670 nm and appearing red in DFM). A large set of distinct SERS spectra (1400 spectra) of citrate were observed in time-dependent SP-SERS measurements. Each spectrum took about 2 s for measurement, which includes spectrum accumulation, data storage, and a dwell time (1 s) before collecting the next spectrum. Due to the large number of distinct spectra, a cluster analysis (CA) algorithm was used to group the spectra. Two types of groups were observed from the CA, which were termed as favorable (F) and probable (P) spectra based on their likelihood of appearance and intensities. F-spectra appeared frequently (number of spectra > 5) in temporal SERS, whereas P-spectra appeared less than five times. Theoretical simulations were performed to model binding modes of citrate on the Ag(111) surface, and the Raman spectra were computed, which were compared with the experimental spectral groups. Additional investigations on understanding the changes in the vibrational frequencies were performed using isotopically labeled (2,2,4,4-d_4-deuterated) citrate-protected AgNPs. Each of the distinct spectra of citrate gave complementary pieces of information about its structure and variants. This systematic analysis of distinct spectra of ligands using SP-SERS and DFM in conjunction with computations may lead to a vibrational tomography (VT) of ligands and understand details of one of the most ubiquitous NPs, including their ligand shell with their details of adsorbate structure. We note that the term VT is used here to indicate the approach that resembles slicing of an object (ligand) through several orientations and reconstructing its three-dimensional structure. However, the structure reconstructed is that of the ligands and their orientations using VT, and a detailed picture of the core of the nanoparticle can be obtained only via electron microscopy. Combined inputs from electron microscopy and VT may be used to reconstruct the complete 3D picture of the NPs.

MATERIALS AND METHODS

Materials. TSC dihydrate (>99%) was purchased from Merck Life Science Private Limited. Silver nitrate (99.9%) was purchased from RANKEM, India. 3-(Mercaptopropyl)-trimethoxysilane was purchased from Sigma-Aldrich. Deuterated citric acid was purchased from Cambridge Isotopes Laboratories, Inc. Other reagents were of analytical grade and used without further purification. Deionized water (DI; ∼18.2 MΩ) obtained from Milli-Q was used throughout the experiments.

Synthesis of Citrate-Capped Silver Nanoparticles. AgNP sols were synthesized using the modified Turkevich method.[32,33] Briefly, $AgNO_3$ (17 mg in 100 mL of DI water) solution was heated to boil, and then trisodium citrate (40 mg in 2 mL of DI water) was added. Once the color of the solution changed to pale yellow, it was quenched under tap water. The formation of AgNPs was confirmed by UV−vis spectroscopy, transmission electron microscopy (TEM), and DFM. Synthesized AgNPs were polydispersed in size, and their shape was confirmed by imaging techniques.

Immobilization of Nanoparticles. The immobilization of AgNPs on the glass slide was done by the pinpoint immobilization method. Briefly, an ultrasonically cleaned 1 mm thick glass slide (SCHOTT) was flushed with 5 mL of a solution of (3-mercaptopropyl)trimethoxysilane (2 μM in ethanol). Then it was washed extensively with ethanol twice to remove excess MPTMS, followed by DI water. About a 10 μL dispersion of NPs was drop-casted and covered with a clean glass coverslip for 30 min of incubation. After incubation, the coverslip was removed and the glass slide was washed extensively with DI water to remove the unbound NPs. Then, 2 μL of DI water was dropped on the immobilized region and covered with a 0.145 mm thick Nexterion cleanroom cleaned coverslip. It was sealed with nail paint on the sides to avoid drying of samples. In the overall procedure, care was taken to expose only one side of the slide to chemicals.

Instrumentation. UV−visible spectroscopic measurements were performed using a PerkinElmer Lambda 25 spectrophotometer in the range of 200−1100 nm. TEM measurements were performed using a JEOL 3010, 300 kV instrument. Samples were spotted on carbon-coated copper grids by drop-casting followed by drying in ambient air. Field emission scanning electron microscopy (FESEM) measurements were performed using a Thermo Scientific Verios G4 UC SEM having a retractable detector.

Single-Particle Imaging and Confocal Raman Microspectroscopy Setup for SP-SERS. Home-built dark-field assisted confocal Raman microspectroscopy (DF CRMS) setup was used for single-particle measurements. Immobilized NPs were first focused with Dage Excel M cooled CCD camera with the help of a Cytoviva high-resolution dark-field condenser and Olympus 100× oil immersion objective. Time-dependent SP-SERS spectra were collected with a WITec GmbH confocal Raman microscope equipped with 632.8 nm (He−Ne gas) laser having an output power of 650 μW on the sample for monitoring red-colored AgNPs. This instrument was equipped with an Olympus BX41 optical microscope and a thermoelectrically cooled charge-coupled detector (ANDOR CCD Detection System) with a 1024 × 1024 pixel format, operating at −80 °C. The initial signals were calibrated using the 520 cm^{-1} vibrational mode of silicon with 100× air objective. A total of 150 grooves/mm grating was used for collecting plasmonic scattering spectra

https://dx.doi.org/10.1021/acs.jpcc.0c09981
J. Phys. Chem. C 2021, 125, 3553−3566

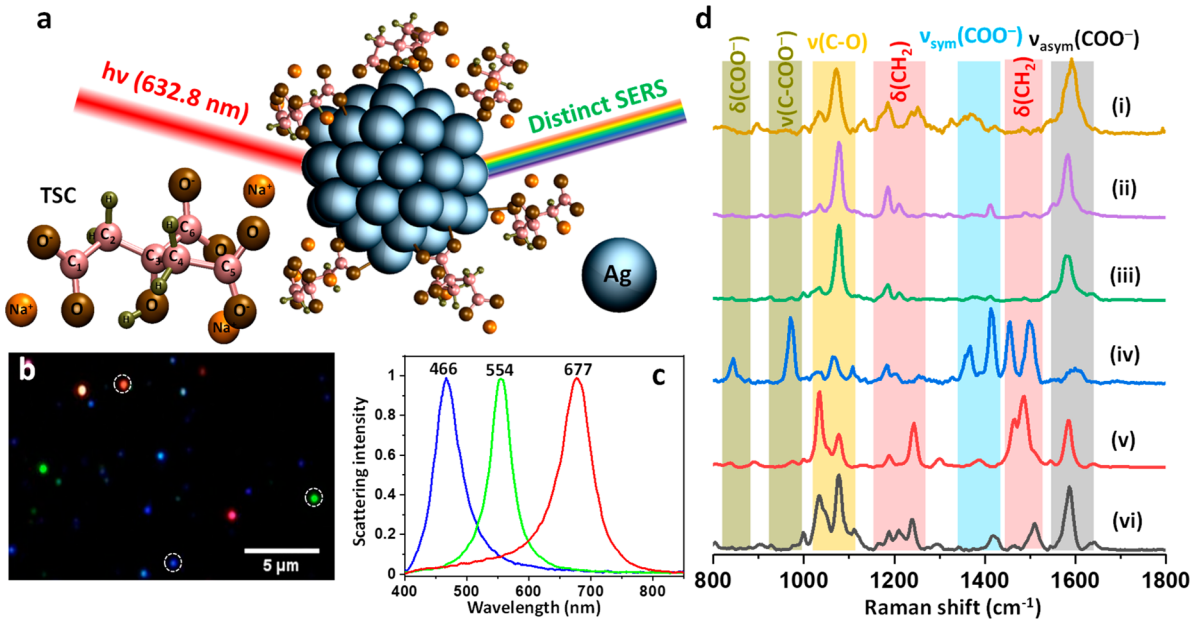

Figure 1. (a) Schematic representation of the interaction of citrate-capped AgNP with an excitation laser leading to the appearance of distinct SP-SERS spectra, (b) plasmonic hyperspectral image, (c) plasmonic scattering spectra (normalized) of immobilized citrate-capped AgNPs, spectra of encircled individual nanoparticles (b) are shown in (c), and (d) distinct SP-SERS spectra of citrate (i–vi) obtained during time-dependent measurements (colored bands correspond to vibrational modes of adsorbed species, and each distinct spectrum belongs to various binding modes and structures of citrate). An individual TSC and a silver atom are also shown in (a).

of AgNPs and 600 grooves/mm was used for SERS measurements. Acquisition time was 1 s throughout the time-dependent experiments.

SP-SERS Spectral Collection. For the SP-SERS spectral collection, the following steps were undertaken:

- At first, an individual red particle was focused using the dark-field camera with a white light source. Then, its plasmonic scattering spectrum was collected.
- Then a white light was switched off, followed by the irradiation of the laser on the same particle, and time-dependent SERS spectra were collected with the measurement time of 2 s.
- Time-dependent spectra were collected for 200–400 s per particle.
- The laser was then turned off, and finally, the plasmonic scattering spectrum of the same particle was collected.
- The above-mentioned sequence was repeated for all the red particles that were monitored for SP-SERS.

Peak Fitting of SP-SERS Spectra. Peak fitting of SP-SERS spectra were performed by using the OriginPro 2020b (Learning Edition, OriginLab Corporation, Northampton, MA, U.S.A.) software. In a nonlinear fitting, under the category of peak functions, the Gaussian function was chosen for peak fitting. The best fit was adapted by selecting parameters (base, center, fwhm, and area of peaks) in such a way that minimized the deviations of the experimental spectra, compared to fitted plots. Multiple iterations of χ-square were performed to converge the fit.

Data Processing and Cluster Analysis. Data processing and analysis were performed using Matlab 2016 (Mathworks) and IJ toolkit plugins of ImageJ.[34] Baseline correction and peak fitting of spectra were done in the origin. The spectra were vector normalized for better comparison and band assignments.

Theoretical Calculations. The structures and interactions of a citrate molecule on the surface of a AgNP were studied computationally by considering a few simplified model systems such as a small piece of the surface that was cut out from a bulk Ag crystal along the (111) plane to largely mimic the facets of Ag NPs. The geometry optimizations were performed in the real space density functional theory (DFT) with the projector augmented wave method (PAW), as implemented in GPAW,[35,36] using the PBE functional.[37] The PAW setup was used as Ag ($4d^{10}5s^1$), O ($2s^22p^4$), C ($2s^22p^2$), H ($1s^1$), and Na ($3s^1$), with scalar-relativistic effects included for Ag. The geometry optimizations of the Ag nanocluster and surface were kept fixed and carried out with a grid spacing of 0.2 Å and minimizing the residual forces without any symmetry constraints by 0.05 eV/Å.

Further, DFT calculations were performed using the B3LYP/6-31+G(d) functional/basis set, as implemented in the Gaussian 09 package.[35,37] The structures of global and local minima (stable and transition structures) were optimized with the B3LYP density functional. The 6-31+G(d) basis set was adopted for C, H, O, and Na, whereas the Ag atom was described by the LANL2DZ basis set and the associated effective core potential, which was demonstrated to be a suitable choice to describe the reactivity of the metal centers. The calculated vibrational spectra of the citrate molecule were compared with the experimental spectra, and the main peaks were identified. The calculated harmonic vibrational frequencies were typically larger than the fundamental frequencies observed experimentally and therefore have to be scaled according to the method and basis set used. The determination of appropriate scale factors for estimating fundamental experimental frequencies from theoretical harmonic frequencies has received considerable attention in the literature.[38] The scaling factor for B3LYP/6-31+G(d), as obtained from the literature, was 0.95.[39]

RESULTS AND DISCUSSION

Distinct Spectra of Citrate Obtained During SP-SERS. Visualizing NPs at the single-particle level and understanding

https://dx.doi.org/10.1021/acs.jpcc.0c09981
J. Phys. Chem. C 2021, 125, 3553–3566

the nature of ligands on the particle surface are important in the development of ligand-stabilized NPs.[15] Laser-induced plasmon tuning and the subsequent appearance of SERS in single AgNPs were demonstrated in our recent work, where a simultaneous study of plasmonic spectroscopy and Raman scattering was performed using a custom-built DFM-coupled confocal Raman microspectrometer.[32] To conduct the present work, a similar setup with modifications in the excitation source and dark field condenser was used. A schematic and a photograph of the experimental setup are presented in Figure S1, which is capable of measuring the plasmonic scattering spectra of single NPs and time-dependent SERS spectra of the capped ligands on them, sequentially. Citrate-capped AgNPs used for SP-SERS were characterized by UV−visible absorption spectroscopy and TEM (Figure S2). Out of all the immobilized AgNPs, red-colored AgNPs, as seen under DFM, were monitored selectively with an excitation source (632.8 nm) at 1.3 μW incident (0.5 μW absorbed) power per NP. Laser power calculations incident/absorbed per NP are explained in the Supporting Information (SI). AgNPs were selected such that their plasmonic scattering band (640−670 nm) was at slightly higher wavelength with respect to the Raman excitation wavelength. This was done to overlap the high energy shoulder of the plasmon with the Raman excitation and downward molecular vibronic transitions, which results in better SERS activity.[40] This is one of the conditions for the on-resonance state of SERS.[32,40] The LSPR spectrum in the range of 640−670 nm in the plasmonic hyperspectral imaging corresponds to the scattering property of selected individual NPs, whereas the LSPR band centered around 419 nm in the UV−visible spectrum corresponds to the absorption property of the bulk colloid. To understand the distribution of immobilized individual AgNPs and their interparticle spacing, we have performed FESEM of immobilized AgNPs on conducting glass slide (ITO-coated transparent glass slide with dimensions, 76 × 26 × 1.1 mm, similar to HSI glass slide). Single NPs and small aggregates of 2−3 particles were observed in such FESEM images, and these were considered as individual NPs (Figure S3). For the immobilized AgNPs used for SP-SERS, the particle density and interparticle distance calculations derived from them were performed using DFM images shown in Figure S4. Further verification of such individual particles was performed using plasmonic scattering spectroscopy.

In the past, various aggregating agents like mineral acids and salts have been used to enhance SERS signals of citrate, using citrate-capped AgNPs.[17,41] Unlike previous reports, we have successfully acquired time-dependent SP-SERS spectra of citrate in the absence of aggregating agents. This was possible due to the particle dynamics-induced plasmon-enhanced Raman scattering (PDI-PERS) phenomenon.[32] A schematic shown in Figure 1a shows the appearance of distinct spectra from an individual citrate-capped AgNP due to PDI-PERS. Immobilized individual AgNPs were characterized by plasmonic hyperspectral imaging and spectroscopy (Figure 1b,c). Distinctly different spectra (Figure 1d) were obtained during time-dependent SERS. To understand these distinct spectra of citrate (Figure 1d), we investigated the vibrational bands of TSC experimentally and theoretically. DFT optimized structure of TSC and simulated Raman spectrum of the same are presented in comparison to the experimental spectrum (Figure S5). A good match between the simulated and experimental spectra of TSC was observed (Figure S5a). Five major bands in the range of 750−2000 cm^{-1} were present in the Raman spectrum of TSC. Band assignments and the various modes of vibrations are displayed in Figure S5a and S5b, respectively. Assignments (Table S1) of distinct SERS spectra of citrate (Figure 1d) were made with the help of the simulated Raman spectrum of TSC (Figure S5a) and existing literature on the SERS of citrate.[14,17,19,42] Each contrasting color band in Figure 1d corresponds to a specific vibrational mode of citrate. Vibrational markers of the carboxylate group of citrate corresponding to $\upsilon_{asym}(COO^-)$ and $\upsilon_{sym}(COO^-)$ were present in the regions of 1560−1640 and 1350−1420 cm^{-1}, respectively, depicted in gray and blue bands. Dominant intensities of $\upsilon_{asym}(COO^-)$ and $\upsilon_{sym}(COO^-)$ vibrations in the spectra showed the binding between the COO^- group and the Ag surface. The third important band lies in the region of 1050−1100 cm^{-1}, which corresponds to υ(C−O). Bending vibrations of $\delta(COO^-)$ appeared at 820−870 cm^{-1}, while stretching vibrations of (C−COO) appeared at 930−980 cm^{-1}. These were weak or absent in the SP-SERS spectra, although they were intense in a typical Raman spectrum. This was attributed to the tilting of COO^- group with respect to the Ag surface in the adsorbed state.[17] Bands at 1130−1170 and 1440−1480 cm^{-1} were assigned to CH_2 vibrations.

Distinct SP-SERS spectra (Figure 1d, i−vi) displayed variations in their peak positions and intensities that have been correlated to the different binding modes and intermediates of citrate. To ensure that these distinct features were only from citrate or its derived species but not from the immobilizing agent, that is, (3-mercaptopropyl)-trimethoxysilane (MPTMS), we performed a control experiment where AgNPs were drop-casted without MPTMS and used for SP-SERS. Similar vibrational features (Figure S6) were observed in the absence of MPTMS, which confirmed that the peaks arose from citrate. Additional data were obtained using deuterated citrate (to be presented later). Plasmonic scattering spectra and DFM images of AgNPs monitored before and after laser exposure are shown in Figure S7. Changes in the color of AgNPs are attributed to laser-induced particle reshaping and reorientation of NPs, as reported previously.[32] To avoid significant heating effects on NPs, we have performed experiments at a low laser power of ∼1.3 μW per NP (particle size was 50 ± 10 nm). Insights obtained from the distinct SP-SERS spectra of citrate are discussed in the sections below.

CA of Time-Dependent SP-SERS Spectra. We monitored 25 individual red-colored particles, as seen in DFM images (Figure S7) for time-dependent SP-SERS. Some were SERS active (20%), and others were inactive (80%). A total of 1400 spectra, each with a measurement time of 2 s were collected from SERS active NPs (five particles). Although we have monitored as many as 25 particles for SP-SERS, only 20% of all NPs were SERS active since SERS is highly specific, and citrate is a nonresonant molecule. Also, monitoring SP-SERS of AgNPs with similar plasmonic scattering spectra from heterogeneous sample is challenging and tricky. We have done statistical analysis of SERS spectra obtained from SERS-active NPs and not on all the NPs. We obtained 1400 SERS spectra on which cluster analysis was performed to understand the variability in spectra corresponding to the orientations of the ligand. Since we have monitored a large set of time-dependent SERS spectra, the issue of statistical reliability arising from a small set of SERS-active NPs is not important for the conclusions drawn. To gain insights into the molecular information from a large set of spectra, a CA algorithm[34,43] was applied for statistical grouping. The algorithm groups or classifies the random SP-SERS spectra into clusters or groups of similar spectra. A cluster is a set of

https://dx.doi.org/10.1021/acs.jpcc.0c09981
J. Phys. Chem. C 2021, 125, 3553−3566

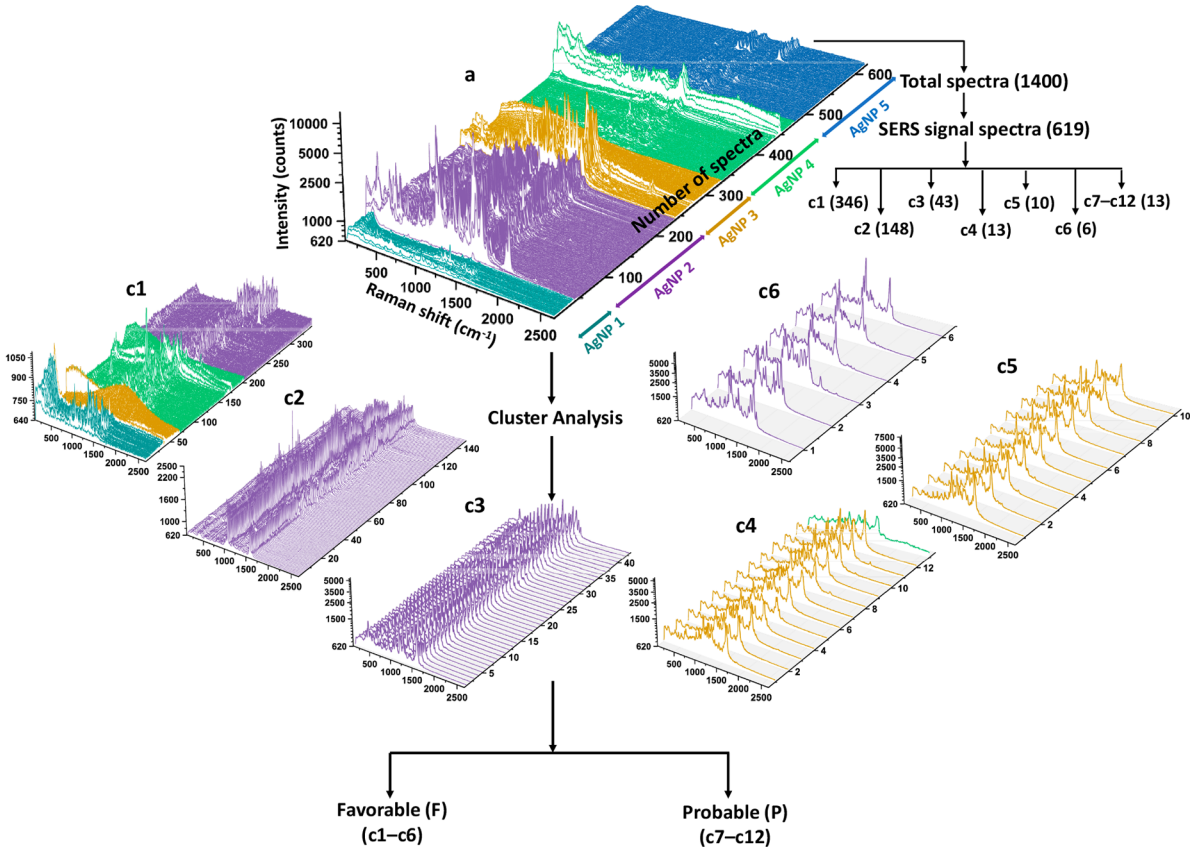

Figure 2. CA of time-dependent SP-SERS spectra leading to multiple spectral collections. (a) Waterfall stack of 619 spectra obtained from five individual AgNPs, where the *z*-axis indicates the number of spectra that are color coded for each AgNP under observation. c1−c6 and c7−c12 represent various clusters that consist of spectra based on their similarity after CA of (a). Finally, two subgroups, termed as F and P spectra, were obtained from different clusters based on their likelihood of appearance and intensities (see text).

entities, which are alike, based on specific features.[44] These spectra were used for CA, and the algorithm was run with various parameters such as tolerance limit, randomization seed, and noise threshold.[34] These technical terms, CA code, and the sequence of steps followed for running the algorithm have been explained in the SI, clustering methods and algorithms. All the spectra (1400) were grouped to 15 clusters. When more than 15 clusters were chosen, it resulted in the generation of certain identical clusters. We observed that when fixed values of the cluster center tolerance limit, randomization seed, noise-threshold, and same set of spectra and number of clusters were taken while running CA, it resulted in the same pattern of clusters, indicating that such clustering is representative of the set.

Two major categories were observed in CA based on the value of noise-threshold. One category corresponded to those spectra, which were above a noise-threshold, and others were below the threshold. The intensity of the signals was measured in terms of counts. The category with the intensity of signals of more than 80 contained 619 spectra displayed in Figure 2a. Each colored spectral group (Figure 2a) originated from an individual particle. Various colors in Figure 2 indicate a set with spectra obtained from five individual AgNPs. It is important to have some idea about the morphology and nature of the SERS-yielding AgNPs. It is equally important to know which types of orientations are preferred for which individual NPs. Hence, to have information about AgNPs and the orientations of citrate arising from the former, we have grouped SP-SERS spectra with high S/N in different clusters with various colors.

The remaining 781 spectra (Figure S8) out of 1400 belonged to a second category with intensities below the noise-threshold. Some spectra composed of cosmic rays also appeared that possessed sharp spikes and spurious features having a line width typically narrower than Raman bands.[45] Such cosmic rays/spikes[45] were removed from the signal spectra. It was done to avoid interference from such peaks in the spectral assignment.

Distinct spectra observed were shown in the waterfall plot (Figure 2a). In the set of 15 clusters, 3 clusters with 781, 35, and 5 spectra belonged to blank, broad, and noisy spectra, respectively (Figure S8). From the remaining 12 clusters, 6 clusters possessed 346, 148, 43, 13, 10, and 6 spectra, as shown in Figure 2 (c1−c6), and the other 6 clusters (c7−c12) possessed 4, 4, 2, 1, 1, and 1 spectra, respectively, presented in Figure S9. These 12 clusters possess spectra with better S/N and were further classified into two subgroups as F and P spectra based on their likelihood of appearance and intensities. An overview of the CA process is outlined in Figure 2.

Analysis of Structural Models of Citrate: F and P Spectra. The first group (F-spectra) with six clusters contained spectra with the probability of appearance greater than 1% (i.e., number of spectra > 5 per cluster) and had intensities in the range of 100−2000 counts. The other group (P-spectra) also possessed six clusters, where each cluster contained less than five spectra and had intensities in the range of 2000−12000. When adsorbates are present on the more uniform surfaces of NPs, they may give SERS with lower intensities but when they are present at hotspots, such as vertices or grooves, higher intensities could occur.[46] Also, enhanced signal intensity in P-spectra

https://dx.doi.org/10.1021/acs.jpcc.0c09981
J. Phys. Chem. C 2021, 125, 3553−3566

Table 1. Various Binding Modes of $-COO^-$ Group of Citrate[a]

S. No.	Type of bond vibration	Coordination	Schematic representation
(1)	$\nu_{asym}(COO^-) > \nu_{sym}(COO^-)$	Unidentate (η^1)	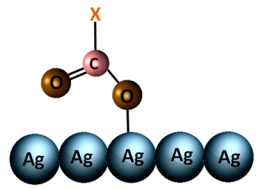
(2)	$\nu_{sym}(COO^-) > \nu_{asym}(COO^-)$	Bidentate (η^2)	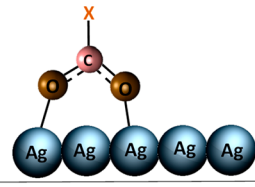
(3)	$\nu_{sym}(COO^-) > \nu_{asym}(COO^-)$	Bridging (μ)	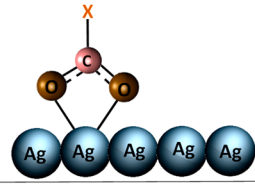

[a]X attached with $-COO^-$ indicates the remaining structure of citrate.

Scheme 1. Photodecarboxylation of Citrate to Acetonedicarboxylate in a Two-Step Process Due to the Presence of α-OH Group and Laser-Induced Plasmon Heating[a]

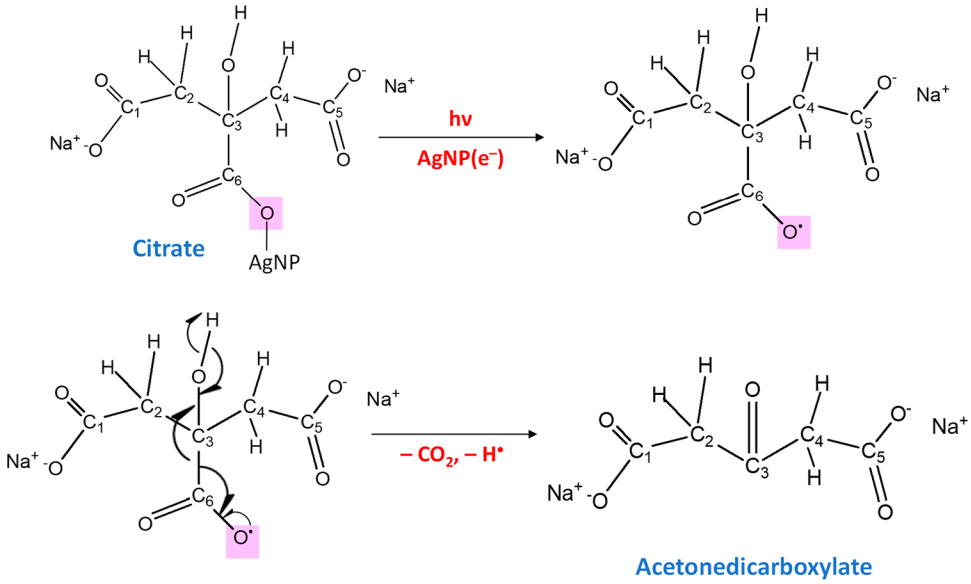

[a]Photolysis produces a free electron at both the C_6OO and the AgNP, which are shown. The product, acetonedicarboxylate, is bound to AgNPs.

compared to F-spectra is likely to be due to the laser-induced reshaping of AgNPs with time that leads to the preferential appearance of hotpots on the NP surface.[32] Chemical enhancement (CE) process that arises due to the formation of charge transfer complexes between the ligands and NPs are very likely to contribute to SERS intensity fluctuations. The contribution of CE may result in further enhancement of SERS intensities giving rise to the SERS-probable spectra. According to the literature, various binding modes of citrate such as unidentate (η^1),[11,19,41] bidentate (η^2),[7,11,19] bridging (μ),[11,15,19] combination (η^1, η^2, μ), and photodecomposed products[47,48] are reported. A list of all the η^1, η^2, and μ binding modes of one of the carboxylate (COO^-) of citrate is presented in Table 1.

An OH group in the α-position of carboxylic acid/carboxylate (Scheme 1) is known to enhance photodecarboxylation reaction, because this group can be transformed into an aldehyde or ketone group by two consecutive electron-transfer reactions.[49] Photodecarboxylation of citrate to acetonedicarboxylate has been described with the schematic shown below (Scheme 1). In such photodecarboxylation, along with the removal of CO_2, $H^\bullet$ is also produced. Understanding of the fate of $H^\bullet$ on the surface of AgNPs is elusive at present, and we have not attempted to study this.

https://dx.doi.org/10.1021/acs.jpcc.0c09981
J. Phys. Chem. C 2021, 125, 3553−3566

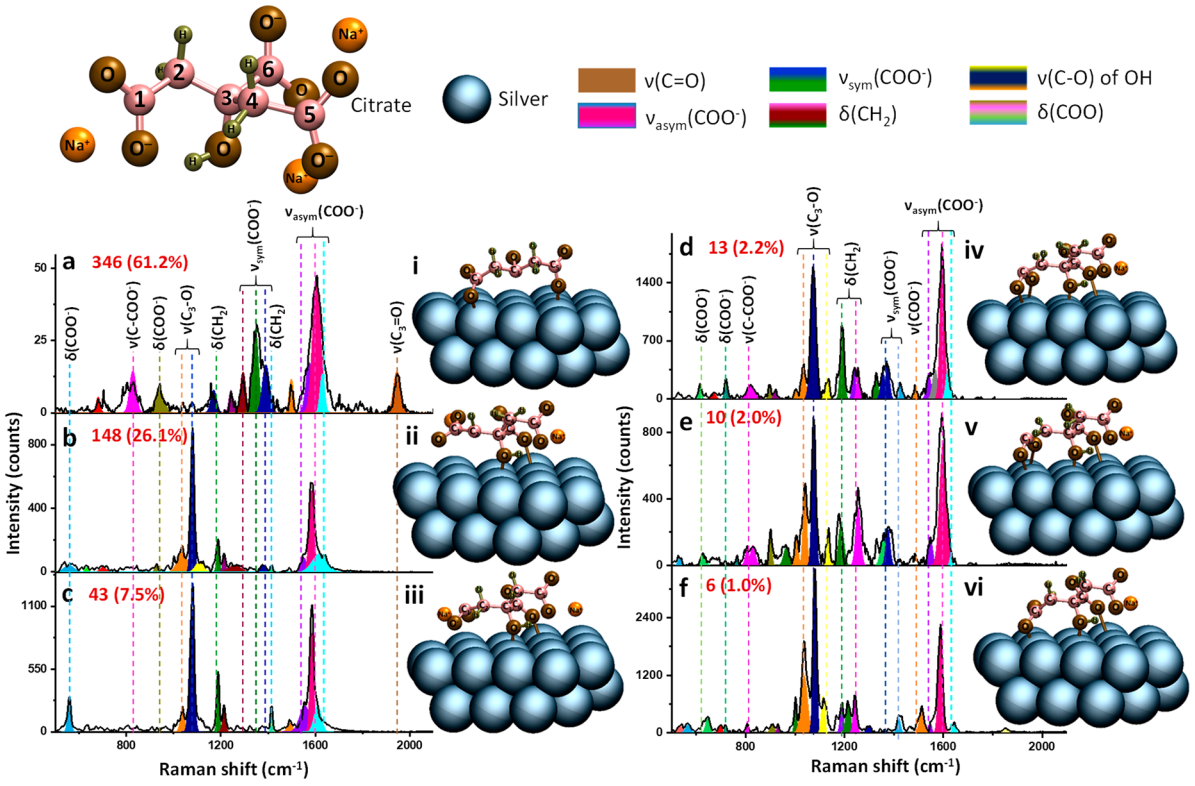

Figure 3. F-spectra with the percentage of spectral populations (a–f) and the corresponding structural models (i–vi) as insets. Specific features of relevance in each spectrum are indicated. TSC, silver atom, and vibrational bands are shown at the top. All six carbon atoms are numbered in TSC. Vibrational modes are color-coded.

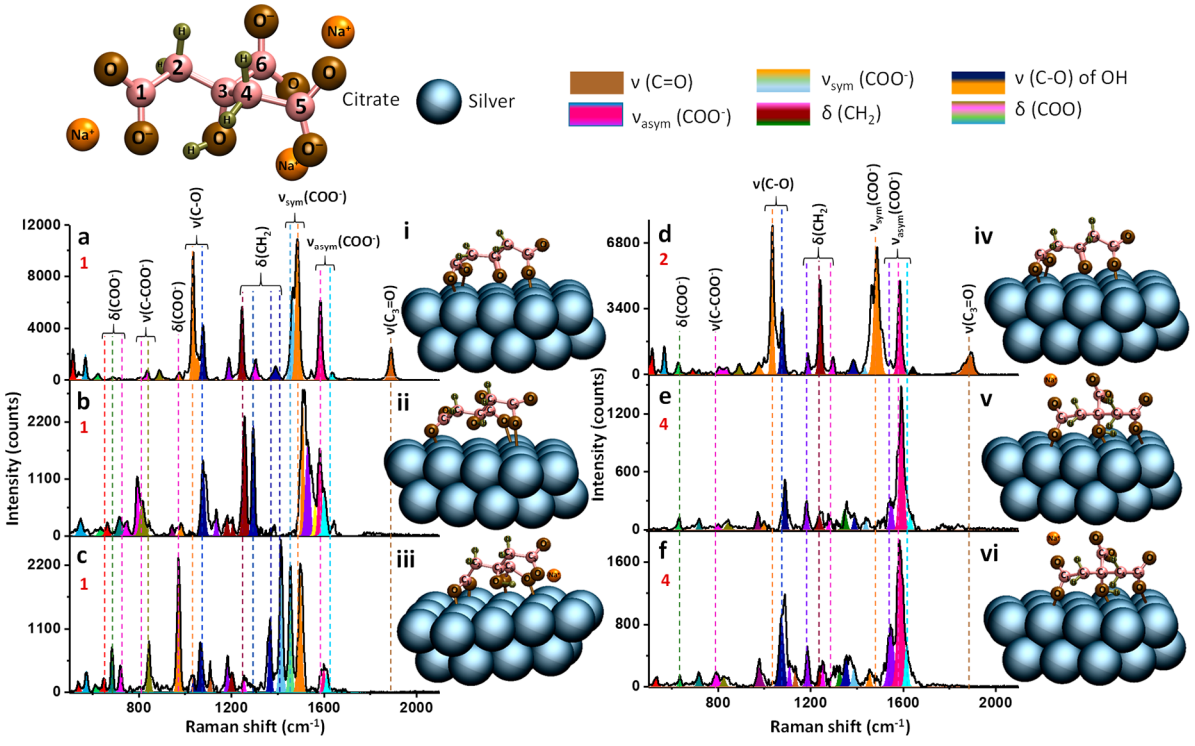

Figure 4. P-spectra and the number of their spectral populations (a–f), with the corresponding structural models (i–vi). Specific features of relevance in each spectrum are indicated. TSC, silver atom, and vibrational bands are shown at the top. All six carbon atoms are numbered in TSC. Vibrational modes are color-coded.

Citrate, a complex molecule possesses six carbon atoms with three COO^- and one α-OH group. Three COO^- groups are positioned as C_1 (terminal), C_5 (terminal), and C_6 (central), as shown in Scheme 1. The α-OH group is attached to C_3 as C_3–O.

https://dx.doi.org/10.1021/acs.jpcc.0c09981
J. Phys. Chem. C 2021, 125, 3553–3566

Different adsorbate models were proposed based on the existing literature[11−16,18,19,47] and new DFT simulations. In the analysis sequence, at first, peak fitting of the F and P spectra (Figure 3 and Figure 4) was performed to evaluate the changes in the vibrational bands. Details about the peak fitting are discussed in the Materials and Methods section. Later, intensity differences of COO^-, C−O, and CH_2 peaks were considered to propose different binding modes and structures of citrate. In all the spectra, peak intensities of $\upsilon_{asym}(COO^-)$ vibrations were stronger than $\upsilon_{sym}(COO^-)$, suggesting that unidentate coordination of COO^- (η^1) with Ag surface was largely preferred in SP-SERS.[14,41] In contrast, higher intensity of $\upsilon_{sym}(COO^-)$ indicates the bidentate or bridging (η^2 or μ) coordination. In the proposed models and DFT simulations of adsorbate structures, when COO^- was bound with the Ag surface, Na^+ attached with the specific COO^- was neglected that satisfies the coordination of COO^- with Ag surface and charge balance. Proposed models corresponding to the spectra are discussed below.

F-Spectra. In the case of F-spectra, two types of spectra were observed dominantly. In the first type (Figure 3a), the peak corresponding to $\upsilon(C_3-O)$ was absent while in the other (Figure 3b−f) it was present. Peak intensity of $\upsilon(C_3-O)$ was higher than $\upsilon_{asym}(COO^-)$ in the spectra (Figure 3b,c,e,f), except in Figure 3d, where the intensity ratio was the reverse. Moreover, $\upsilon_{asym}(COO^-)$ vibrations were stronger than $\upsilon_{sym}(COO^-)$ in all spectra (Figure 3a−f).

In the first spectrum (Figure 3a) of the F category, $\upsilon_{asym}(COO^-)$ being dominant over $\upsilon_{sym}(COO^-)$, indicated the η^1 binding mode for C_1, C_5, and C_6 carboxylates.[41] However, a peak at 1946 cm^{-1} corresponding to $\upsilon(C_3{=}O)$ was observed that arises due to the photodecarboxylation of C_6OO^-, as shown in Scheme 1.[47] The third major peak at 1080−1120 cm^{-1} due to $\upsilon(C_3-O)$ of α-OH was absent, which indicated no direct interaction of C_3-O with the Ag surface.[19] Hence, the structural model in Figure 3a(i) with η^1 of C_1OO^-, C_5OO^-, and $\upsilon(C_3{=}O)$ was favored for the first spectrum (Figure 3a). This model contributes about 61.2% (346 spectra) of the total population (619 spectra) of SP-SERS. Spectra with photodecarboxylation is dominant. Due to localized plasmon heating, photodecarboxylated species can appear more even when the laser power is low.

In the spectrum of Figure 3b, the appearance of a peak at 1074−1080 cm^{-1} corresponds to direct interaction of $\upsilon(C_3-O)$ with the surface. The absence of the 1946 cm^{-1} peak indicates that this spectrum is devoid of decarboxylated species (Scheme 1). As $\upsilon_{asym}(COO^-)$ is stronger than $\upsilon_{sym}(COO^-)$, the η^1 mode is favored for C_1, C_5, and C_6. The absence of peaks in the region of 1345−1385 cm^{-1} suggests C_1OO^- and C_5OO^- away from the Ag surface. Thus, a model corresponding to η^1 of C_6OO^- and $\upsilon(C_3-O)$ interacting with Ag surface is shown in Figure 3b(ii). This model contributes to 26.1% (148 spectra) of the total population.

The spectrum of Figure 3c is similar to Figure 3b, with the only differences in enhanced intensities of peaks at ∼1200 and ∼1400 cm^{-1}. These features are due to CH_2 vibrations and the enhanced intensity suggests that CH_2 groups vibrate perpendicular to the Ag surface. A new peak at 558 cm^{-1} is present, which is due to $\delta(COO^-)$.[17] Hence, the structural model of citrate for the spectrum in Figure 3c is similar to Figure 3b, with CH_2 groups perpendicular to the Ag surface and this model contributes 7.5% (43 spectra) to the total population.

In Figure 3d, four new peaks appear at 720, 820, 1324, and 1364 cm^{-1}, which are due to $\delta(COO^-)$ and $\upsilon_{sym}(COO^-)$. These vibrations arise when COO^- is in the η^2 mode.[7,11,41] With the presence of $\delta(COO^-)$, we may suggest that either of the C_1OO^- and C_5OO^- remain away from the Ag surface. The higher intensity of $\upsilon_{asym}(COO^-)$ than $\upsilon_{sym}(COO^-)$ favors η^1 binding of C_6OO^-. Thus, we propose η^2 of C_1OO^- and η^1 of C_6OO^-, along with $\upsilon(C_3-O)$ binding with the Ag surface, and the corresponding structural model is presented in Figure 3d(iv). This model contributes to 2.2% (13 spectra) of the total population.

Figure 3e is similar to Figure 3d with slight variations in $\delta(CH_2)$ vibrations. These variations do not cause much change in the COO^- binding, rather the orientation of the CH_2 groups gets affected. The structural model is presented as Figure 3e(v), and it contributes 2.0% (10 spectra) to the total population.

The spectrum in Figure 3f has a new peak at 1508 cm^{-1}, which is due to the $\upsilon_{asym}(COO^-)$. This arises due to the η^1 binding of the terminal carboxylates (C_1OO^- and C_5OO^-). Other peaks at ∼1080 cm^{-1} and the weak intensity of ∼1380 cm^{-1} are due to $\upsilon(C_3-O)$ and η^1 of C_6OO^-. With the presence of $\delta(COO^-)$, we suggest that either of the C_1OO^- and C_5OO^- remain away from the Ag surface. Hence, η^1 for both C_1OO^- and C_6OO^-, and $\upsilon(C_3-O)$ are proposed for this spectrum, and a model is presented in Figure 3f(vi) that contributes to 1% of the total SP-SERS.

P-Spectra. In the P group (Figure 4) also, two types of spectra were observed. In the first type, the intensity of $\upsilon_{sym}(COO^-)$ was higher than $\upsilon_{asym}(COO^-)$ and $\upsilon(C_3-O)$, favoring η^2 and μ (Figure 4a,c,d) binding modes of COO^-, while in the second type, $\upsilon_{asym}(COO^-)$ vibrations were stronger than $\upsilon_{sym}(COO^-)$ and $\upsilon(C_3-O)$ (Figure 4b,e,f), favoring the η^1 binding mode.

In Figure 4a, the combination of $\upsilon_{sym}(COO^-)$ and $\delta(CH_2)$ vibrations that appear at 1388, 1462, and 1486 cm^{-1} were higher in intensity than $\upsilon_{asym}(COO^-)$ at 1584 cm^{-1}, indicating the η^2 mode of C_1OO^-, C_5OO^-, and C_6OO^-. However, the presence of 1890 cm^{-1} peak corresponds to $\upsilon(C_3{=}O)$ (Scheme 1). Also, two other peaks at 1033 and 1078 cm^{-1} due to $\upsilon(C-O)$ were present. The intense peak at 1033 cm^{-1} indicates the coupling of C−O with CH_2 vibrations. Thus, η^2 of C_1OO^- with η^1 of C_5OO^- and $\upsilon(C_3{=}O)$ are favored for this spectrum, and the corresponding adsorbate model is presented as Figure 4a(i). This spectrum appeared only once during the time-dependent spectra.

The spectrum in Figure 4b has $\upsilon_{asym}(COO^-)$ as a dominant feature with multiple peaks at 1512, 1530, 1585, and 1602 cm^{-1}, respectively, which indicate η^1 binding for all the three COO^- groups. Peaks around ∼1380−1420 cm^{-1} due to $\upsilon_{sym}(COO^-)$ are absent. Enhanced $\delta(CH_2)$ features indicate that these vibrate perpendicular to the surface, and the peak intensity at ∼1077 cm^{-1} is weak, which supports weaker interaction of $\upsilon(C_3-O)$ with the surface. Thus, η^1 of C_1OO^-, C_5OO^-, and C_6OO^- are favored for the spectrum, and the corresponding structure is shown in Figure 4b(ii). This spectrum also appeared once during SP-SERS.

In Figure 4c, $\upsilon_{sym}(COO^-)$ peaks are more dominant than $\upsilon_{asym}(COO^-)$, indicating the η^2 mode for C_1OO^-, C_5OO^-, and C_6OO^-. The presence of a strong peak at 970 cm^{-1} is due to $\delta(COO^-)$, leading to terminal carboxylates (C_1OO^-/C_5OO^-) away from the surface. The absence of the 1080 cm^{-1} peak depicts no binding of $\upsilon(C_3-O)$ with the surface. The structural model having a η^2 binding of C_1OO^- and C_6OO^- with C_5OO^- remaining unbound is presented in Figure 4c(iii). This spectrum also appeared once in the set.

https://dx.doi.org/10.1021/acs.jpcc.0c09981
J. Phys. Chem. C 2021, 125, 3553−3566

Table 2. Summary of Spectral Probability of Occurrence, Vibrational Features, Assignments, and Their Corresponding Binding Modes of Citrate Attributed to F and P Spectra

subgroup (type of cluster)	probability of occurrence/total SERS spectra (619)	major vibrational peaks (cm^1; intensity counts*)	vibrational assignments	binding modes	figures and structures
F(c1)	346	1605 > 1389, 1948	$\upsilon_{asym}(COO^-) > \upsilon_{sym}(COO^-)$, decarboxylated-$\upsilon(C_3{=}O)$	η^1 of C_1OO^- and C_5OO^-	Figure 3a,a(i)
F(c2)	148	1585, 1081, 1187 (227*), 1385 (absent)	$\upsilon_{asym}(COO^-$, $\upsilon(C_3{-}O)$, and $\delta(CH_2)$	η^1 of C_6OO^- and $\delta(CH_2)$	Figure 3b,b(ii)
F(c3)	43	1585, 1081, 1187 (553*), 1385 (absent)	$\upsilon_{asm}(COO^-)$, $\upsilon(C_3{-}O)$, and $\delta(CH_2)$	η^1 of C_6OO^- and $\delta(CH_2)$ $\perp$ to Ag surface	Figure 3c,c(iii)
F(c4)	13	720, 820, 1324, 1586 > 1364, 1077, 1187 (885*)	$\upsilon_{asym}(COO^-) > \upsilon_{sym}(COO^-)$, $\delta(COO^-)$, $\upsilon(C_3{-}O)$, and $\delta(CH_2)$	η^1 of C_6OO^-, η^2 of C_1OO^- and $\delta(CH_2)$ $\perp$ to Ag surface	Figure 3d,d(iv)
F(c5)	10	720, 820, 1324, 1586 > 1364, 1077, 1187 (250*)	$\delta(COO^-)$, $\upsilon_{asym}(COO^-) > \upsilon_{sym}(COO^-)$, $\upsilon(C_3O)$, and $\delta(CH_2)$	η^1 of C_6OO^-, η^2 of C_1OO^- and $\delta(CH_2)$	Figure 3e,e(v)
F(c6)	6	720, 820, 1508, 1586, 1077	$\delta(COO^-)$, $\upsilon_{asym}(COO^-) > \upsilon_{sym}(COO^-)$ and $\upsilon(C_3{-}O)$	η^1 of C_1OO^- and C_6OO^-	Figure 3f,f(vi)
P(c7)	4	1585 > 1364, 1077	$\upsilon_{asym}(COO^-) > \upsilon_{sym}(COO^-)$ and $\upsilon(C_3{-}O)$	η^1 of C_1OO and C_5OO^-	Figure 4f,4f(ui)
P(c8)	4	1586 > 1364, 1077	$\upsilon_{asym}(COO^-) > \upsilon_{sym}(COO^-)$ and $\upsilon(C_3{-}O)$	η^1 of C_1OO and C_5OO^-	Figure 4e,e(v)
P(c9)	2	1035 (10100*), (1388 and 1462 > 1486 and 1584), 1890	$\upsilon(C_3{-}O) + \delta(CH_2)$, $\upsilon_{sym}(COO)$ > $\upsilon_{asym}(COO^-)$, $\delta(CH_2)$, and decarboxylated-$\upsilon(C_3{=}O)$	η^2 of C_1OO^- and η^1 of C_5OO^-	Figure 4d,d(iv)
P(c10)	1	(1365 and 1412 > (1586 and 1612), (1454, 1497), (720, 820, 970)	$\upsilon_{sym}(COO^-) > \upsilon_{asym}(COO^-)$, $\delta(CH_2]$, and $\delta(COO^-)$	η^3 of C_1OO^- and C_6OO^-	Figure 4c,c(iii)
P(c11)	1	1512, 1530, 1584, 1253, and 1293	$\upsilon_{asym}(COO^-) > \upsilon_{sym}(COO^-)$ and $\delta(CH_2)$	η^1 of C_1OO^-, C_5OO^-, C_6OO^-, and $\delta(CH_2)$ $\perp$ to Ag surface	Figure 4b,b(ii)
P(c12)	1	1035 (7700*), (1388 and 1462 > 1486 and 1584), 1890	$\upsilon(C_3{-}O) + \delta(CH_2)$, $\upsilon_{sym}(COO^-)$ > $\upsilon_{asym}(COO^-)$, $\delta(CH_2)$, and decarboxylated-$\upsilon(C_3{=}O)$	η^2 of C_1OO^- and η^1 of C_5OO^-	Figure 4a,a(i)

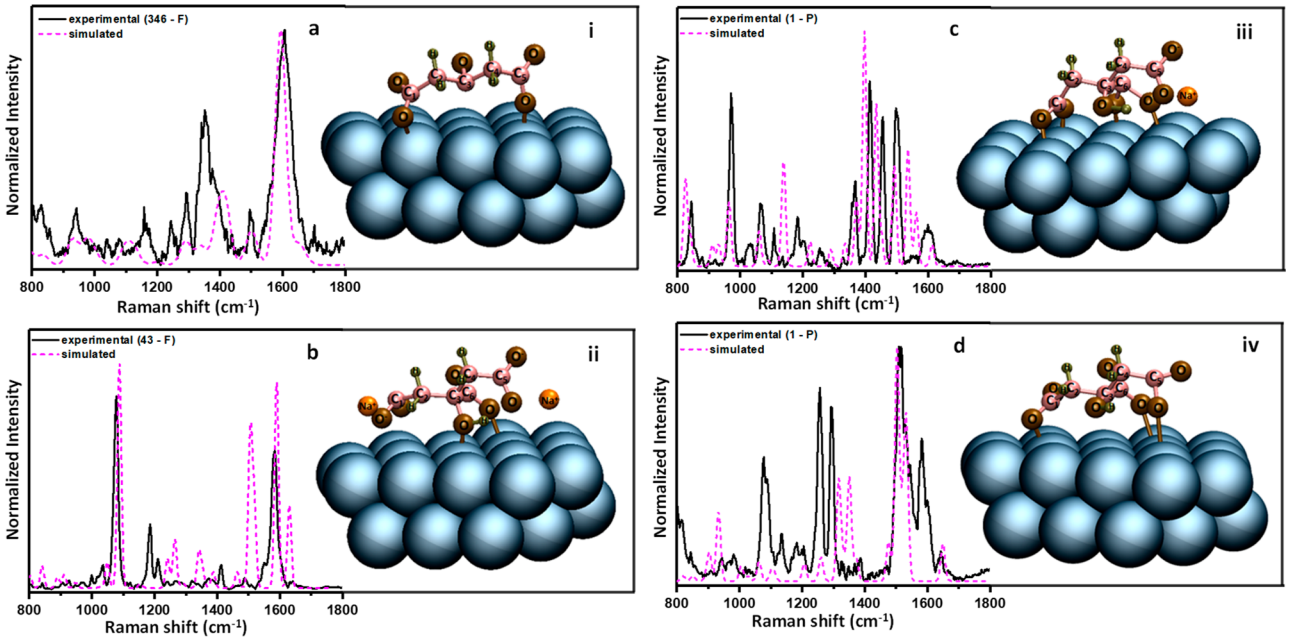

Figure 5. Comparison between simulated and experimental (F and P) spectra (a–d) and their corresponding optimized structures (i–iv) with various binding modes of COO^- and C–O. Simulated spectra of a, b, c, and d correspond to F-346 (Figure 3a), F-43 (Figure 3c), P-1 (Figure 4c), and P-1 (Figure 4b) spectra, respectively.

Figure 4d is similar to Figure 4a, with the only difference in intensities of 1585 and 1030 cm^{-1}. In the spectrum in Figure 4d, the 1030 cm^{-1} peak is more intense than that at 1585 cm^{-1}, while the spectrum in Figure 4a has the reverse. This indicates that $\upsilon(COO^-)$ and $\upsilon(C_3{-}O)$ are the same as shown in the structure shown in Figure 4a(i). However, slight variations are observed in the orientation with respect to the surface. This spectrum appeared twice in the set.

The spectra in Figure 4e,f have similar features with variations in peak intensities of ~1580 and ~1077 cm^{-1}. As the $\upsilon_{asym}(COO^-)$ peak is dominant over $\upsilon_{sym}(COO^-)$, we propose a structure with η^1 binding of C_1OO^- and C_5OO^-. The presence of the ~1077 cm^{-1} peak confirms the binding of $\upsilon(C_3{-}O)$ with the surface. Hence, the structural model having η^1 of C_1OO^-, C_5OO^- with $\upsilon(C_3{-}O)$ is presented in the insets of Figure 4e(v) and f(vi). These spectra (Figure 4e,f) appeared four times in the set.

https://dx.doi.org/10.1021/acs.jpcc.0c09981
J. Phys. Chem. C 2021, 125, 3553–3566

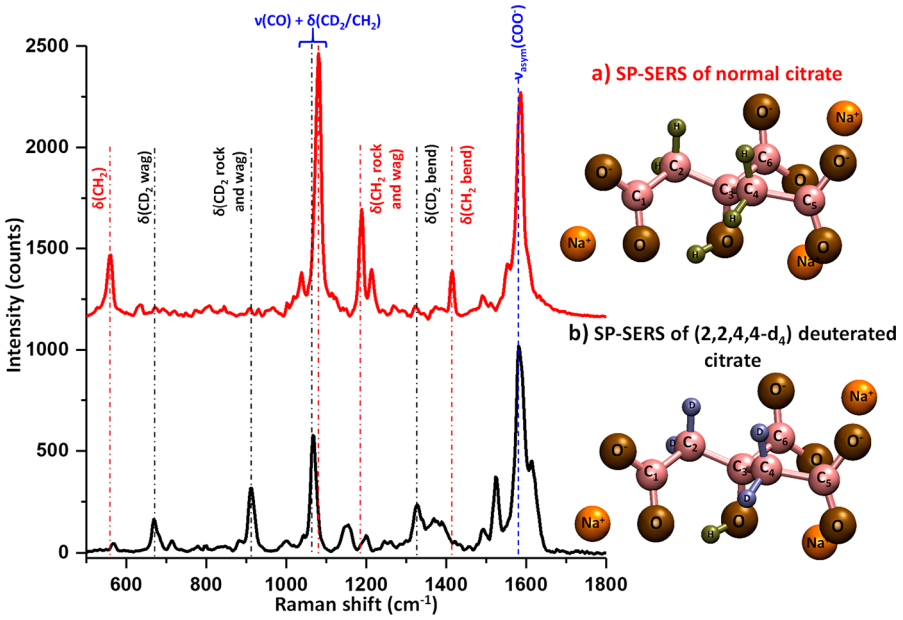

Figure 6. Comparison of SP-SERS spectra of normal citrate-capped AgNPs (a) and deuterated citrate-capped AgNPs (b). Structural models corresponding to normal citrate and deuterated citrate are shown next to the spectra. Spectral assignments are marked with dotted lines.

Scheme 2. Schematic Representation of Various Ligand Geometries of Citrate on the Crystallographic Planes of AgNPs, Shown in Two Tomographic Arrangements (I and II)[a]

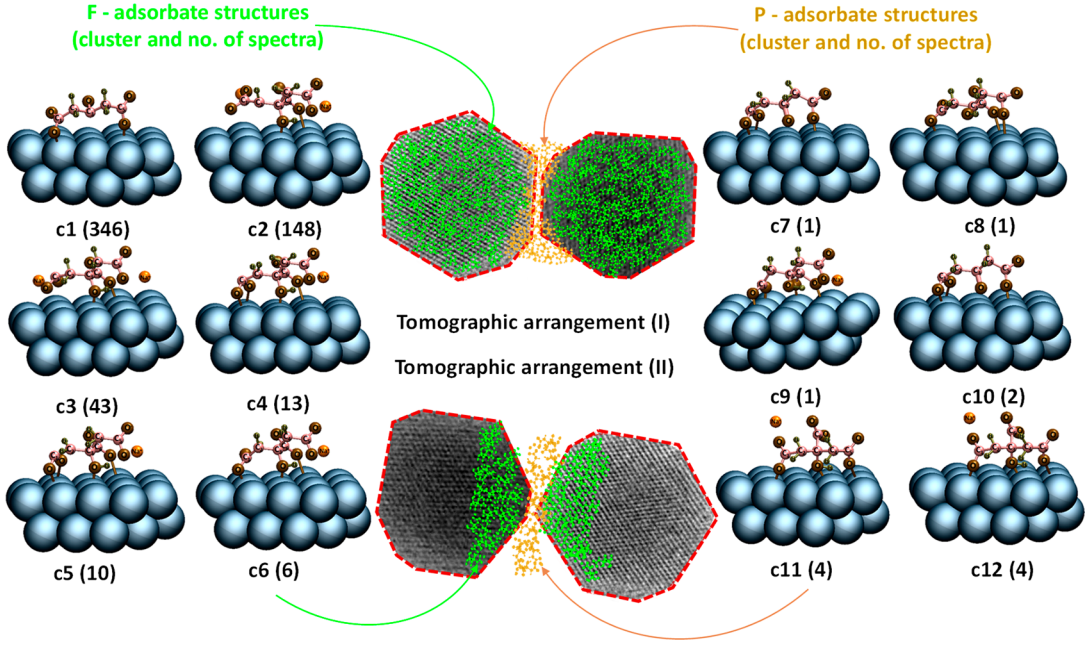

[a]A combination of all these structures lead to VT of citrate. The images of AgNPs shown are selected from HRTEM data and are used for illustrative purposes.

To make it easier for the reader to correlate the data, a summary of all the binding modes of citrate occurring in the two subgroups of F and P spectra are tabulated in Table 2.

Based on the proposed models, these structures were simulated according to the bonding interactions of the COO^- and α-OH groups to the NP surface, namely, η^1, η^2, and μ coordination or a combination of these. Interaction of citrate with the surface of AgNP was studied computationally by considering a few simplified model systems, such as a surface that was cut out from the bulk Ag crystal along the (111) plane, to largely mimic one of the facets of AgNPs. Frequency calculations were performed to assess the nature of $\upsilon(COO^-)$ and $\upsilon(C_3-O)$. The simplified model surface with 25 silver atoms provide sufficient space to accommodate all the possible interactions of citrate over the Ag surface. Although a larger model would have been considered, a lesser number of Ag atoms also made it feasible to conduct vibrational frequency calculations. Coordinates of the optimized structures of citrate, Ag_{55}, Ag_{25}, and Ag_{25}–citrate structures are mentioned in the Appendices of the SI. Four structures of citrate with different

https://dx.doi.org/10.1021/acs.jpcc.0c09981
J. Phys. Chem. C 2021, 125, 3553−3566

binding modes and a comparison between the experimental and simulated spectra, corresponding to F and P groups are presented in Figure 5a−d. The spectra displayed a positive correlation between the simulated and the experimental spectra with optimized structures of citrate as insets. It is evident that simulated spectra were sensitive toward the binding of COO^- with the Ag surface, through η^1, η^2, and μ coordination. The binding mode η^1 was favorable than η^2 and μ in most of the optimized structures (Figure 5).

However, some discrepancies were observed between the experimental and theoretical spectra, which are attributed to factors such as geometrical discrepancies between simulated models and experimentally accessible NPs, neglecting the influence of water present as a medium and larger surface coverage of citrate. The differences in experimental and simulated spectra could also be due to an admixture of binding modes of citrate for which there was no feasible way to perform simulations.

Insights about Citrate Binding Modes Using Isotopically Labeled Citrate-Capped AgNPs. In order to confirm that such modes of vibrations are due to citrate and variants of photocatalyzed products, time-dependent SP-SERS experiments were performed also with deuterated AgNPs. Deuterated citrate (2,2,4,4-d_4) was used for the synthesis of deuterium-labeled AgNPs using the modified Turkevich method.[33]

Synthesized deuterated AgNPs were characterized by UV−vis absorption spectroscopy, TEM, DFM, and plasmonic scattering spectroscopy (Figure S10). A comparative Raman plot was made between normal and deuterated TSC to understand the vibrational shifts appearing in the C and D vibrations (Figure S11). A similar CA was performed on the time-dependent SP-SERS of deuterated citrate-capped AgNPs, which resulted in two subgroups (F and P) according to their likelihood of spectral appearance and intensities (Figure S12). A comparative SP-SERS plot between deuterated and normal citrate is presented in Figure 6 to understand the changes in the vibrational bands described. Major features corresponding to $\upsilon_{asym}(COO^-)$ and υ(C−O) modes were present at similar peak positions in deuterated citrate-capped AgNPs as in normal AgNPs. However, variations were observed in CH_2 and CD_2 vibrations, marked with dotted lines in Figure 6.

A schematic below (Scheme 2) explains the various binding modes of citrate we have identified on dynamically changing individual AgNPs.

The center of the schematic has AgNPs capped with citrate molecules in two possible orientations (I and II) with varying hotspots and SERS favorable conditions. In one arrangement, adsorbates are present in-between the NPs (hotspot) and on the surface, while in the other arrangement, adsorbates are available at the hotspots and locations near the hotspots where strong plasmonic coupling takes place. Adsorbates present at the hotspot belong to the P-category, while adsorbates on the surface of NP or the places surrounding the hotspots belong to the F-category. A combination of all these multitude of orientations and binding modes help to reconstruct the three-dimensional structure of citrate on the surface of AgNPs, leading to VT of citrate-protected nanoparticles. Data collection and reconstruction of these orientations are similar to the steps used in tomographic reconstruction. Such a study can be used to probe the changing ligand geometry during changes in the particle, such as that which could occur during particle reconstruction upon laser-irradiation. Many of these binding modes and orientations of citrate may have been influenced by the change in temperature due to laser-induced heating. Most of the ligand structure information we have obtained corresponds to room temperature. However, some of the orientations may have arisen due to increased local plasmonic heating.[32] However, the incident laser power of 1.3 μW per NP is far less than the laser power (0.1−60 mW) used for other studies to evaluate local temperature (100−2000 K).[50−53] Richard-Lacroix and Deckert have reported that under SERS/TERS conditions, local temperature cannot be quantified exactly via the Boltzmann equation alone, and the antiStokes/Stokes ratio depends on more factors and not exclusively temperature.[50] Moreover, in the case of SP-SERS for polydisperse AgNPs, there are fluctuations caused in the SERS intensity with different locations of hotspots that makes it challenging to evaluate the localized temperature using the scattering ratio of antiStokes and Stokes lines. However, this is a way forward to evaluate the dependence of ligand orientations on the increase of temperature due to the localized plasmonic heating using coherent antiStokes Raman spectroscopy (CARS).[51] But, with fast spectral acquisition and enhanced computational capabilities and with improved models it will be possible to understand each one of the binding geometries existing on the nanoparticle surface. This knowledge will be useful in reconstructing the most of the ligand geometries possible on the nanoparticle, leading to VT of ligands at the single-particle level.

Limitations and Solutions of the Technique. Some of the limitations associated with the existing SP-SERS and VT techniques and their possible solutions are mentioned below.

1 The imaging of AgNPs by DFM-coupled confocal Raman microspectrometer lacks information about the morphology of AgNPs, but correlative FESEM with the above-mentioned integrated technique can be performed to precisely define the time-dependent morphology of NPs.
2 Several efficient software are available to match Raman spectrum of the unknown sample with the existing library of Raman spectra. Similarly, some library of orientations of a specific molecule can be developed to obtain an immediate 3D picture or reconstruct ligand on the surface of NPs.
3 Particle reshaping after performing time-dependent SERS leads to changes in NP but that gives mobility to ligands to adsorb at different facets for different orientations. However, better SERS-active and stable NPs with ligands having multitude of orientations can be utilized to work efficiently with the reconstruction and VT of ligands.

■ CONCLUSIONS

In this work, we have analyzed time-dependent SP-SERS spectra of citrate adsorbed on AgNPs. Studies were performed with 632.8 nm excitation at 1.3 μW incident power per NP. SP-SERS played an important role in capturing the rare adsorbate structures and intermediates of analytes on the NP surface. We performed CA on temporal SERS spectra to simplify and organize a set 1400 distinct spectra. This resulted in two subgroups of spectra based on their likelihood of appearance and intensities. The first group (F-spectra) where each cluster possessed spectral populations greater than 1% of the total and another (P-spectra) that contained below 1% of the spectra. These distinct spectra were correlated to the different binding modes, structures, and photocatalyzed variants of citrate adsorbed on the AgNP surface. Various binding modes were proposed, and DFT simulations were performed on them

https://dx.doi.org/10.1021/acs.jpcc.0c09981
J. Phys. Chem. C 2021, 125, 3553−3566

generating distinct spectra. The η^1 binding was more favorable than η^2 and μ binding of COO^- in most of the SP-SERS spectra. Sodium citrate (2,2,4,4-d_4) capped AgNPs were used to confirm the variations observed in the vibrational features. We demonstrated the general background and rationale for the development of VT of ligands protected nanoparticles with the necessary experimental and theoretical tools.

■ ASSOCIATED CONTENT

Supporting Information

The Supporting Information is available free of charge at https://pubs.acs.org/doi/10.1021/acs.jpcc.0c09981.

Figures S1−S12, Table S1, calculations SI−SII, Code I, references, and appendices (PDF)

■ AUTHOR INFORMATION

Corresponding Author

Thalappil Pradeep − *DST Unit on Nanoscience, Thematic Unit of Excellence, Department of Chemistry, Indian Institute of Technology Madras, Chennai 600036, India;* orcid.org/0000-0003-3174-534X; Phone: +91044-2257-4208; Email: pradeep@iitm.ac.in

Authors

Tripti Ahuja − *DST Unit on Nanoscience, Thematic Unit of Excellence, Department of Chemistry, Indian Institute of Technology Madras, Chennai 600036, India*

Kamalesh Chaudhari − *DST Unit on Nanoscience, Thematic Unit of Excellence, Department of Chemistry, Indian Institute of Technology Madras, Chennai 600036, India*

Ganesan Paramasivam − *DST Unit on Nanoscience, Thematic Unit of Excellence, Department of Chemistry, Indian Institute of Technology Madras, Chennai 600036, India*

Gopi Ragupathy − *DST Unit on Nanoscience, Thematic Unit of Excellence, Department of Chemistry, Indian Institute of Technology Madras, Chennai 600036, India*

Jyoti Sarita Mohanty − *DST Unit on Nanoscience, Thematic Unit of Excellence, Department of Chemistry, Indian Institute of Technology Madras, Chennai 600036, India*

Complete contact information is available at: https://pubs.acs.org/10.1021/acs.jpcc.0c09981

Author Contributions

†These authors contributed equally to this work. T.P. proposed the idea of VT of ligands. T.A., K.C., and T.P. conceived the experiments. T.A. performed all SP-SERS measurements. T.A. did data analysis. K.C. contributed in programming and coding. G.P. and G.R. performed DFT simulations. J.S.M. helped with TEM measurements.

Notes

The authors declare no competing financial interest.

■ ACKNOWLEDGMENTS

We thank the Department of Science and Technology, Government of India for constantly supporting our research activities. T.A. acknowledges an Institute Graduate Fellowship. G.P. is thankful for an Institute Postdoctoral Fellowship. We thank Mr. Amoghavarsha Kini, Mr. Gaurav Vishwakarma, and Mr. Pillalamarri Srikrishnarka for their valuable input in relation to this work.

■ ABBREVIATIONS

AgNPs, silver nanoparticles
SERS, surface-enhanced Raman scattering
SP-SERS, single-particle surface-enhanced Raman scattering
F, favorable
P, probable
DFT, density functional theory
DFM, dark-field microscopy
CRM, confocal Raman microspectroscopy
CA, cluster analysis

■ REFERENCES

(1) Henglein, A.; Giersig, M. Formation of Colloidal Silver Nanoparticles: Capping Action of Citrate. *J. Phys. Chem. B* **1999**, *103*, 9533−9539.

(2) Grzelczak, M.; Pérez-Juste, J.; Mulvaney, P.; Liz-Marzán, L. M. Shape Control in Gold Nanoparticle Synthesis. *Chem. Soc. Rev.* **2008**, *37*, 1783−1791.

(3) Ke, F.; Qiu, L.; Yuan, Y.; Jiang, X.; Zhu, J. Fe_3O_4 Nanoparticles Were Synthesized by a Solvothermal Method as Reported Previously. *J. Mater. Chem.* **2012**, *125*, 1−8.

(4) Wu, G.-W.; He, S.-B.; Peng, H.-P.; Deng, H.-H.; Liu, A.-L.; Lin, X.-H.; Xia, X.-H.; Chen, W. Citrate-Capped Platinum Nanoparticle as a Smart Probe for Ultrasensitive Mercury Sensing. *Anal. Chem.* **2014**, *86*, 10955−10960.

(5) Ojea-Jiménez, I.; López, X.; Arbiol, J.; Puntes, V. Citrate-Coated Gold Nanoparticles as Smart Scavengers for Mercury(II) Removal from Polluted Waters. *ACS Nano* **2012**, *6*, 2253−2260.

(6) Choi, C. K. K.; Chiu, Y. T. E.; Zhuo, X.; Liu, Y.; Pak, C. Y.; Liu, X.; Tse, Y. L. S.; Wang, J.; Choi, C. H. J. Dopamine-Mediated Assembly of Citrate-Capped Plasmonic Nanoparticles into Stable Core-Shell Nanoworms for Intracellular Applications. *ACS Nano* **2019**, *13*, 5864−5884.

(7) Grys, D.-B.; de Nijs, B.; Salmon, A. R.; Huang, J.; Wang, W.; Chen, W.-H.; Scherman, O. A.; Baumberg, J. J. Citrate Coordination and Bridging of Gold Nanoparticles: The Role of Gold Adatoms in AuNP Aging. *ACS Nano* **2020**, *14*, 8689−8696.

(8) Xie, H.; Tkachenko, A. G.; Glomm, W. R.; Ryan, J. A.; Brennaman, M. K.; Papanikolas, J. M.; Franzen, S.; Feldheim, D. L. Critical Flocculation Concentrations, Binding Isotherms, and Ligand Exchange Properties of Peptide-Modified Gold Nanoparticles Studied by UV - Visible, Fluorescence, and Time-Correlated Single Photon Counting Spectroscopies. *Anal. Chem.* **2003**, *75*, 5797−5805.

(9) Lin, S.-Y.; Tsai, Y.-T.; Chen, C.-C.; Lin, C.-M.; Chen, C.-h. Two-Step Functionalization of Neutral and Positively Charged Thiols onto Citrate-Stabilized Au Nanoparticles. *J. Phys. Chem. B* **2004**, *108*, 2134−2139.

(10) Polte, J.; Ahner, T. T.; Delissen, F.; Sokolov, S.; Emmerling, F.; Thunemann, A. F.; Kraehnert, R. Mechanism of Gold Nanoparticle Formation in the Classical Citrate Synthesis Method Derived from Coupled in Situ XANES and SAXS Evaluation. *J. Am. Chem. Soc.* **2010**, *132*, 1296−1301.

(11) Glusker, J. P. Citrate Conformation and Chelation: Enzymatic Implications. *Acc. Chem. Res.* **1980**, *13*, 345−352.

(12) Monti, S.; Barcaro, G.; Sementa, L.; Carravetta, V.; Ågren, H. Characterization of the Adsorption Dynamics of Trisodium Citrate on Gold in Water Solution. *RSC Adv.* **2017**, *7*, 49655−49663.

(13) Floate, S.; Hosseini, M.; Arshadi, M. R.; Ritson, D.; Young, K. L.; Nichols, R. J. An In-Situ Infrared Spectroscopic Study of the Adsorption of Citrate on Au(111) Electrodes. *J. Electroanal. Chem.* **2003**, *542*, 67−74.

(14) Li, M.; Xiao, Y.; Zhang, Z.; Yu, J. Bimodal Sintered Silver Nanoparticle Paste with Ultrahigh Thermal Conductivity and Shear Strength for High Temperature Thermal Interface Material Applications. *ACS Appl. Mater. Interfaces* **2015**, *7*, 9157−9168.

(15) Al-Johani, H.; Abou-Hamad, E.; Jedidi, A.; Widdifield, C. M.; Viger-Gravel, J.; Sangaru, S. S.; Gajan, D.; Anjum, D. H.; Ould-Chikh,

S.; Hedhili, M. N.; et al. The Structure and Binding Mode of Citrate in the Stabilization of Gold Nanoparticles. *Nat. Chem.* **2017**, *9*, 890−895.
(16) Mikhlin, Y. L.; Vorobyev, S. A.; Saikova, S. V.; Vishnyakova, E. A.; Romanchenko, A. S.; Zharkov, S. M.; Larichev, Y. V. On the Nature of Citrate-Derived Surface Species on Ag Nanoparticles: Insights from X-Ray Photoelectron Spectroscopy. *Appl. Surf. Sci.* **2018**, *427*, 687−694.
(17) Munro, C. H.; Smith, W. E.; Garner, M.; Clarkson, J.; White, P. C. Characterization of the Surface of a Citrate-Reduced Colloid Optimized for Use as a Substrate for Surface-Enhanced Resonance Raman-Scattering. *Langmuir* **1995**, *11*, 3712−3720.
(18) Wulandari, P.; Nagahiro, T.; Fukada, N.; Kimura, Y.; Niwano, M.; Tamada, K. Characterization of Citrates on Gold and Silver Nanoparticles. *J. Colloid Interface Sci.* **2015**, *438*, 244−248.
(19) Park, J. W.; Shumaker-Parry, J. S. Structural Study of Citrate Layers on Gold Nanoparticles: Role of Intermolecular Interactions in Stabilizing Nanoparticles. *J. Am. Chem. Soc.* **2014**, *136*, 1907−1921.
(20) Biggs, S.; Mulvaney, P.; Zukoski, C. F.; Grieser, F. Study of Anion Adsorption at the Gold-Aqueous Solution Interface by Atomic Force Microscopy. *J. Am. Chem. Soc.* **1994**, *116*, 9150−9157.
(21) Lin, Y.; Pan, G.-B.; Su, G.-J.; Fang, X.-H.; Wan, L.-J.; Bai, C.-L. Study of Citrate Adsorbed on the Au(111) Surface. *Langmuir* **2003**, *19*, 10000−10003.
(22) Wulandari, P.; Nagahiro, T.; Michioka, K.; Tamada, K.; Ishibashi, K.; Kimura, Y.; Niwano, M. Coordination of Carboxylate on Metal Nanoparticles Characterized by Fourier Transform Infrared Spectroscopy. *Chem. Lett.* **2008**, *37*, 888−889.
(23) Shi, X.; Li, H.-W.; Ying, Y.-L.; Liu, C.; Zhang, L.; Long, Y.-T. In Situ Monitoring of Catalytic Process Variations in a Single Nanowire by Dark-Field-Assisted Surface-Enhanced Raman Spectroscopy. *Chem. Commun.* **2016**, *52*, 1044−1047.
(24) Nie, S.; Emory, S. R. Probing Single Molecules and Single Nanoparticles by Surface-Enhanced Raman Scattering. *Science* **1997**, *275*, 1102−1106.
(25) Kang, B.; Austin, L. A.; El-Sayed, M. A. Real-Time Molecular Imaging throughout the Entire Cell Cycle by Targeted Plasmonic-Enhanced Rayleigh/Raman Spectroscopy. *Nano Lett.* **2012**, *12*, 5369−5375.
(26) Kang, B.; Austin, L. A.; El-Sayed, M. A. Observing Real-Time Molecular Event Dynamics of Apoptosis in Living Cancer Cells Using Nuclear-Targeted Plasmonically Enhanced Raman Nanoprobes. *ACS Nano* **2014**, *8*, 4883−4892.
(27) Perassi, E. M.; Hrelescu, C.; Wisnet, A.; Döblinger, M.; Scheu, C.; Jäckel, F.; Coronado, E. A.; Feldmann, J. Quantitative Understanding of the Optical Properties of a Single, Complex-Shaped Gold Nanoparticle from Experiment and Theory. *ACS Nano* **2014**, *8*, 4395−4402.
(28) Park, J. W.; Shumaker-Parry, J. S. Strong Resistance of Citrate Anions on Metal Nanoparticles to Desorption under Thiol Functionalization. *ACS Nano* **2015**, *9*, 1665−1682.
(29) Zhang, Z.; Bando, K.; Mochizuki, K.; Taguchi, A.; Fujita, K.; Kawata, S. Quantitative Evaluation of Surface-Enhanced Raman Scattering Nanoparticles for Intracellular PH Sensing at a Single Particle Level. *Anal. Chem.* **2019**, *91*, 3254−3262.
(30) Kleinman, S. L.; Ringe, E.; Valley, N.; Wustholz, K. L.; Phillips, E.; Scheidt, K. A.; Schatz, G. C.; Van Duyne, R. P. Single-Molecule Surface-Enhanced Raman Spectroscopy of Crystal Violet Isotopologues: Theory and Experiment. *J. Am. Chem. Soc.* **2011**, *133*, 4115−4122.
(31) Wilson, A. J.; Willets, K. A. Visualizing Site-Specific Redox Potentials on the Surface of Plasmonic Nanoparticle Aggregates with Superlocalization SERS Microscopy. *Nano Lett.* **2014**, *14*, 939−945.
(32) Chaudhari, K.; Ahuja, T.; Murugesan, V.; Subramanian, V.; Ganayee, M. A.; Thundat, T.; Pradeep, T. Appearance of SERS Activity in Single Silver Nanoparticles by Laser-Induced Reshaping. *Nanoscale* **2019**, *11*, 321−330.
(33) Kimling, J.; Maier, M.; Okenve, B.; Kotaidis, V.; Ballot, H.; Plech, A. Turkevich Method for Gold Nanoparticle Synthesis Revisited. *J. Phys. Chem. B* **2006**, *110*, 15700−15707.
(34) Rueden, C. T.; Schindelin, J.; Hiner, M. C.; DeZonia, B. E.; Walter, A. E.; Arena, E. T.; Eliceiri, K. W. ImageJ2: ImageJ for the next Generation of Scientific Image Data. *BMC Bioinf.* **2017**, *18*, 1−26.
(35) Frisch, M. J.; Trucks, G. W.; Schlegel, H. B.; Scuseria, G. E.; Robb, M. A.; Cheeseman, J. R.; Scalmani, G.; Barone, V.; Mennucci, B.; Petersson, G. A.;et al.*Gaussian*; Gaussian, Inc: Wallingford, CT, 2009.
(36) Yang, Y.; Weaver, M. N.; Merz, K. M. Assessment of the "6-31+Gt; + LANL2DZ" Mixed Basis Set Coupled with Density Functional Theory Methods and the Effective Core Potential: Prediction of Heats of Formation and Ionization Potentials for First-Row-Transition-Metal Complexes. *J. Phys. Chem. A* **2009**, *113*, 9843−9851.
(37) Hehre, W. J. Ab Initio Molecular Orbital Theory. *Acc. Chem. Res.* **1976**, *9*, 399−406.
(38) Sinha, P.; Boesch, S. E.; Gu, C.; Wheeler, R. A.; Wilson, A. K. Harmonic Vibrational Frequencies: Scaling Factors for HF, B3LYP, and MP2Methods in Combination with Correlation Consistent Basis Sets. *J. Phys. Chem. A* **2004**, *108*, 9213−9217.
(39) Merrick, J. P.; Moran, D.; Radom, L. An Evaluation of Harmonic Vibrational Frequency Scale Factors. *J. Phys. Chem. A* **2007**, *111*, 11683−11700.
(40) Zhang, R.; Zhang, Y.; Dong, Z. C.; Jiang, S.; Zhang, C.; Chen, L. G.; Zhang, L.; Liao, Y.; Aizpurua, J.; Luo, Y.; et al. Chemical Mapping of a Single Molecule by Plasmon-Enhanced Raman Scattering. *Nature* **2013**, *498*, 82−86.
(41) Deacon, G. B.; Phillips, R. J. Relationships between the Carbon-Oxygen Stretching Frequencies of Carboxylato Complexes and the Type of Carboxylate Coordination. *Coord. Chem. Rev.* **1980**, *33*, 227−250.
(42) Vinogradova, E.; Tlahuice-Flores, A.; Velazquez-Salazar, J. J.; Larios-Rodriguez, E.; Jose-Yacaman, M. Surface-Enhanced Raman Scattering of N-Acetylneuraminic Acid on Silver Nanoparticle Surface. *J. Raman Spectrosc.* **2014**, *45*, 730−735.
(43) Anil, K. J.; Dubes, R. C. *Algorithms for Clustering Data*; Prentice Hall: Englewood Cliffs, NJ, 1988.
(44) Hu, W.; Duan, S.; Luo, Y. Theoretical Modeling of Surface and Tip-Enhanced Raman Spectroscopies. *Wiley Interdiscip. Rev.: Comput. Mol. Sci.* **2017**, *7*, e1293.
(45) Gautam, R.; Vanga, S.; Ariese, F.; Umapathy, S. Review of Multidimensional Data Processing Approaches for Raman and Infrared Spectroscopy. *EPJ. Technol. Instrum.* **2015**, *2*, 1−38.
(46) Wei, H.; Xu, H. Hot Spots in Different Metal Nanostructures for Plasmon-Enhanced Raman Spectroscopy. *Nanoscale* **2013**, *5*, 10794−10805.
(47) Kumari, G.; Zhang, X.; Devasia, D.; Heo, J.; Jain, P. K. Watching Visible Light-Driven CO2 Reduction on a Plasmonic Nanoparticle Catalyst. *ACS Nano* **2018**, *12*, 8330−8340.
(48) Borer, P.; Hug, S. J.; Sulzberger, B.; Kraemer, S. M.; Kretzschmar, R. Photolysis of Citrate on the Surface of Lepidocrocite: An in Situ Attenuated Total Reflection Infrared Spectroscopy Study. *J. Phys. Chem. C* **2007**, *111*, 10560−10569.
(49) Abrahamson, H. B.; Rezvani, A. B.; Brushmiller, J. G. Photochemical and Spectroscopic Studies of Complexes, of Iron(III) with Citric Acid and Other Carboxylic Acids. *Inorg. Chim. Acta* **1994**, *226*, 117−127.
(50) Richard-Lacroix, M.; Deckert, V. Direct Molecular-Level near-Field Plasmon and Temperature Assessment in a Single Plasmonic Hotspot. *Light: Sci. Appl.* **2020**, *9*, 1−13.
(51) Zhang, C.; Wang, J.; Jasensky, J.; Chen, Z. Molecular Orientation Analysis of Alkyl Methylene Groups from Quantitative Coherent Anti-Stokes Raman Scattering Spectroscopy. *J. Phys. Chem. Lett.* **2015**, *6*, 1369−1374.
(52) Pozzi, E. A.; Zrimsek, A. B.; Lethiec, C. M.; Schatz, G. C.; Hersam, M. C.; Van Duyne, R. P. Evaluating Single-Molecule Stokes and Anti-Stokes SERS for Nanoscale Thermometry. *J. Phys. Chem. C* **2015**, *119*, 21116−21124.
(53) Sun, Y.; Yanagisawa, M.; Kunimoto, M.; Nakamura, M.; Homma, T. Estimated Phase Transition and Melting Temperature of APTES

https://dx.doi.org/10.1021/acs.jpcc.0c09981
J. Phys. Chem. C 2021, 125, 3553−3566

Self-Assembled Monolayer Using Surface-Enhanced Anti-Stokes and Stokes Raman Scattering. *Appl. Surf. Sci.* **2016**, *363*, 572−577.

https://dx.doi.org/10.1021/acs.jpcc.0c09981
J. Phys. Chem. C 2021, 125, 3553−3566